Assimilation of GPS Radio Occultation Refractivity Data with WRF 3DVAR and Its Impact on the Prediction of a Heavy Rainfall Event

JI-HYUN HA

Korea Institute of Atmospheric Prediction Systems, Seoul, South Korea

GYU-HO LIM

Seoul National University, Seoul, South Korea

SUK-JIN CHOI

Korea Institute of Atmospheric Prediction Systems, Seoul, South Korea

(Manuscript received 9 July 2013, in final form 21 January 2014)

ABSTRACT

To accommodate accurate analyses and forecasts of a heavy rainfall event over the Korean Peninsula, the authors assimilated the GPS radio occultation (RO) data by using the Weather Research and Forecasting Model (WRF) and its three-dimensional variational data assimilation system (3DVAR). The employed datasets are from the Constellation Observing System for Meteorology, Ionosphere, and Climate (COSMIC) and Challenging Minisatellite Payload (CHAMP) missions. The selected case was from late October 2006, which intensively hit the northeastern part of the Korean Peninsula with record-breaking rainfall. In this study, the local refractivity observation operator was used in assimilating GPS RO soundings. The results are more pronounced for the cycling assimilation of GPS RO data than for the one-time data assimilation. From all of the parameters investigated (temperature, geopotential height, specific humidity, and winds), the GPS RO soundings highly modified the moisture distribution in the lower troposphere and also changed the wind field via the model dynamics. For the heavy rainfall forecast, the quantitative accuracy of the precipitation forecast with the GPS RO data assimilation was in good agreement with observations in terms of the maximum rainfall amount and threat scores. The improved forecast in the experiment came from the exact positioning of the low pressure system and its consequent convergence near the rainfall area. When RO data and GPS precipitable water data were assimilated simultaneously, the moisture distribution changed horizontally and vertically such that it increased the amount of rainfall, and an accurate description of the convective system development was feasible.

1. Introduction

Global positioning system (GPS) radio occultation (RO) is an active satellite-to-satellite limb sounding technique in which a transmitter and its corresponding receiver are placed on a GPS satellite and on a low-Earth-orbiting (LEO) satellite, respectively. As demonstrated by the proof-of-concept GPS Meteorology (GPS/MET) experiment (Ware et al. 1996), together with the German Challenging Minisatellite Payload (CHAMP; Wickert et al. 2001) and the Argentinean Satélite de Aplicaciones Cientificas-C (SAC-C; Hajj et al. 2004) missions, GPS RO sounding data have many unique characteristics, including high accuracy, high vertical resolution, no need for calibration, all-weather sounding capability, and global coverage. Owing to these characteristics, GPS RO data are ideally suited for climate monitoring and weather prediction, and hence they have played an increasingly important role in climate and meteorology studies (Anthes et al. 2008).

Depending on the level of data processing, a variety of data retrieved from GPS RO can be used for weather prediction (e.g., phase and amplitude of GPS signals,

Denotes Open Access content.

Corresponding author address: Gyu-Ho Lim, Seoul National University, Seoul, 151-747, South Korea.
E-mail: gyuholim@snu.ac.kr

DOI: 10.1175/JAMC-D-13-0224.1

bending angle, refractivity, and retrieved temperature and moisture). Kuo et al. (2000) showed that refractivity and bending angle are likely candidates for practical applications. Wee et al. (2008) investigated the impacts of GPS RO refractivity from the CHAMP and SAC-C missions on the short-range forecasts over the Antarctic using the fifth-generation Pennsylvania State University–National Center for Atmospheric Research Mesoscale Model (MM5) four-dimensional variational data assimilation (4DVAR) system. Chen et al. (2009) assimilated GPS RO refractivity into the Weather Research and Forecasting Model (WRF) and its 3DVAR system using local/nonlocal observation operators to simulate a typhoon that struck Taiwan with torrential rainfall. In addition to these studies, assimilations of GPS RO bending angle and refractivity have shown a positive impact on regional as well as global weather predictions (Kuo et al. 1998; Liu and Zou 2003; Huang et al. 2005; Cucurull et al. 2006; Healy 2008). However, there have been very few studies of the impact of GPS RO data on the ability to forecast hazardous precipitation systems such as a heavy rainfall event.

In this study, we investigated the impact of GPS RO refractivity on simulations of a heavy rainfall event that occurred over the northeastern part of the Korean Peninsula on 22–23 October 2006. This paper serves as a sequel to the earlier studies listed above, with a focus on assessing the impact of GPS RO soundings on the analysis and prediction skill of a short-range forecast system. The outline for the rest of this paper is as follows: section 2 provides the data used for analysis and data assimilation; section 3 presents the synoptic overview of a heavy rainfall case in October 2006, the configuration of the numerical model, and the experiment design; section 4 discusses the analysis and forecast results of this heavy rainfall event; and section 5 offers the summary and conclusions.

2. Data

To analyze the environments of a heavy rainfall event, we employed the global final (FNL) analyses with 1° × 1° horizontal resolution and 26 vertical layers from the National Centers for Environmental Prediction (NCEP), the precipitation dataset from the 75 Korea Meteorological Administration (KMA) stations for the southern Korean Peninsula (marked with the black points in Fig. 2a), and the radar observations. The radar observations were based on 15 radars composing the radar network over the southern Korean Peninsula: 10 sites of the KMA and 5 sites of the Republic of Korea Air Force. Following Park and Lee (2009), we conducted quality control (QC) on the radar data. The QC procedures included alias correction and elimination of abnormal values. For the GPS impact experiments, conventional observations (including radiosonde and surface data) from global telecommunication system (GTS) and GPS RO soundings were used. GPS RO soundings were obtained from the Constellation Observing System for Meteorology, Ionosphere, and Climate/Formosa Satellite Mission 3 (COSMIC/FORMOSAT-3; hereinafter COSMIC) Data Analysis Archival Center in the Binary Universal Format Representation (BUFR) format, which includes the longitude, latitude, and height of the tangent point, and the associated refractivity and azimuth of an incoming ray. COSMIC is a joint mission between Taiwan and the United States in operation since April 2006 with a goal of demonstrating the use of GPS RO data in operational weather prediction, climate analysis, and space weather forecasts. The center has been providing up to 2000 GPS RO soundings per day that are uniformly distributed around the globe. In addition to COSMIC RO soundings, CHAMP RO soundings were also used in this study. CHAMP equipped with GPS receivers was launched in 2000 and has collected 400–500 soundings per day since mid-2001. The distribution of GPS RO soundings used in this study is shown in Fig. 1. They are distributed over the entire model domain, with about 254 soundings from COSMIC (Fig. 1a) and 22 from CHAMP (Fig. 1b). Therefore, there are about 12 times as many COSMIC RO soundings as there are CHAMP RO soundings over the model domain. Figure 1c shows that the number of soundings available for a 6-h time window for 36-h periods (the length of our 3DVAR assimilation window) varies from 7 to 64. It also indicates that GPS soundings are not evenly distributed in time, and more data are available centered at around 0600 UTC.

During an occultation event, the GPS receiver on board an LEO satellite provides accurate measurements of the phase and amplitude of radio signals transmitted by the GPS satellite. These measurements, together with the knowledge of the occulting geometry (i.e., the precise positions and velocities of the GPS and LEO satellites), allow vertical profiles of a ray bending angle to be derived under the assumption of a spherically symmetric refractivity field. The atmospheric refractivity is then retrieved via the Able transform (Phinney and Anderson 1968). Finally, the information on Earth's atmospheric refractivity N can be inferred from temperature T (K), pressure p (hPa), and water vapor pressure e (hPa) after the ionospheric effect is removed in the neutral atmosphere (Smith and Weintraub 1953):

$$N = 77.6\frac{P}{T} + 3.73 \times 10^5 \frac{e}{T^2}. \quad (1)$$

To calculate the innovation during the assimilation procedure, the first-guess fields of temperature, pressure,

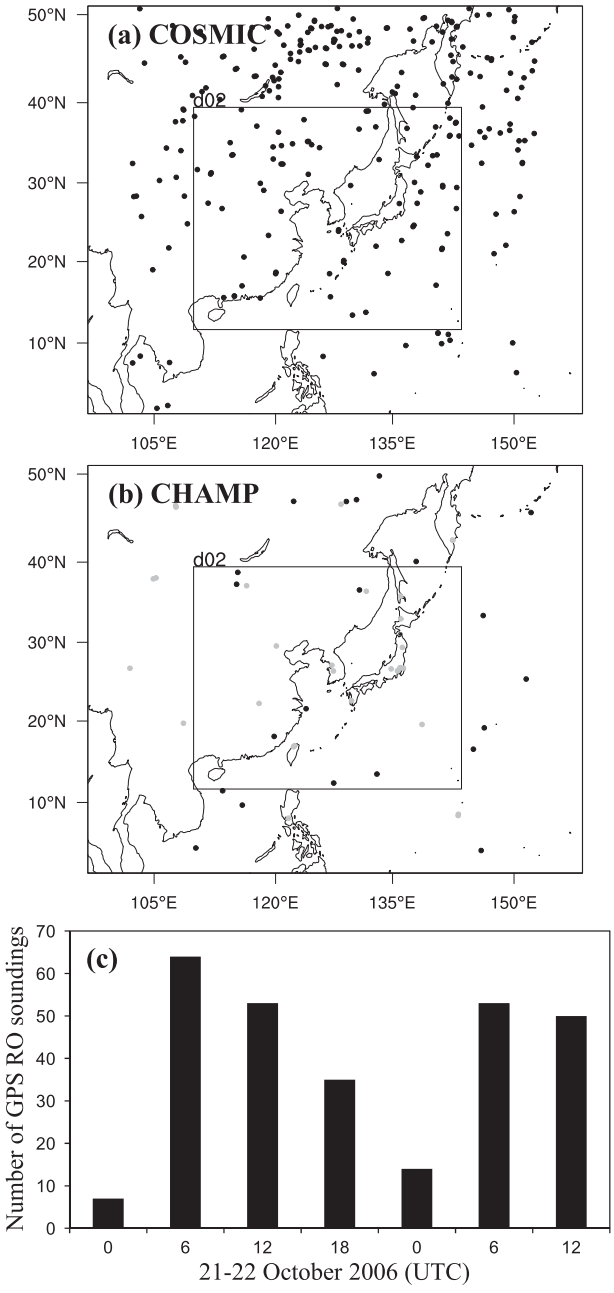

FIG. 1. Distribution of GPS RO soundings from (a) COSMIC (black dots) and (b) CHAMP (black dots) for the period of 0000 UTC 21–1200 UTC 22 Oct 2006. Gray dots in (b) denote the position of the GPS PW observation sites at 1200 UTC 22 Oct 2006. (c) The number of GPS RO soundings as a function of time for each 6-h assimilation window.

and water vapor on the model grid are interpolated to the GPS RO observations' locations, and then the local refractivity is calculated based on Eq. (1). This local refractivity operator is simple and has a low computational cost relative to the nonlocal operator, which is defined as the integrated amount of refractivity along a fixed ray path that may be approximated by a straight line. The disadvantage of the local operator is that it introduces errors over regions with a strong horizontal gradient of refractivity. However, after careful consideration of the strengths and weaknesses of the two methods for our purposes, we decided to use the local operator in the WRF 3DVAR for assimilating the GPS RO refractivity. Besides the datasets from GTS and GPS RO, additional precipitable water (PW) data from the ground-based GPS were used to investigate the impact of simultaneous assimilations of the GPS RO and the ground-based GPS PW datasets. For the PW amount, we obtained the dataset from the International Global Navigation Satellite Systems Service sites and U.S. SuomiNet sites. Their observation locations are marked with the gray points in Fig. 1b.

3. A heavy rainfall case and numerical experiment

a. A heavy rainfall case

The case investigated in this paper is a heavy rainfall event that produced record-breaking rainfall in October 2006 over the northeastern part of the Korean Peninsula. Figure 2a shows the 30-h accumulated rainfall distribution from 1200 UTC 22 to 1800 UTC 23 October and the observed reflectivity (defined as the region with reflectivity greater than 30 dBZ at a height of 3 km) at 1-h intervals from 0200 to 0400 UTC. The rainfall was mostly confined to the northeastern part of the Korean Peninsula where the mountain range with elevations over 1.0 km runs from north to south as shown in Fig. 2b, and the maximum amount of rainfall in Gangneung was roughly 309.5 mm over 30 h. The heavy rainfall was mainly concentrated from 0100 to 0400 UTC 23 October, with a maximum hourly rainfall rate of 64.5 mm h^{-1} at 0200 and 0300 UTC 23 October (Fig. 2c). On the radar image for the intense rainfall period, the strong reflectivity (marked E) corresponded well with the observed heavy rainfall region, and strong reflectivity (marked W) was also found to the west of the rainfall band. From 0200 to 0400 UTC, the cell W moved southward, but the cell E continuously developed near Gangneung, which produced heavy rainfall of approximately 60 mm h^{-1} above Gangneung. A mountain range with an elevation greater than 1.0 km runs between the two cells as shown in Figs. 2a and 2b, and hence topography seemed to play a role in preventing the cell W from propagating eastward, which restrained the cell W to the upstream side of the rainfall band.

Figure 3 shows 500- and 850-hPa weather charts at 1200 UTC 22 and 0000 UTC 23 October, which is about 14 and 2 h before the time of maximum hourly rainfall,

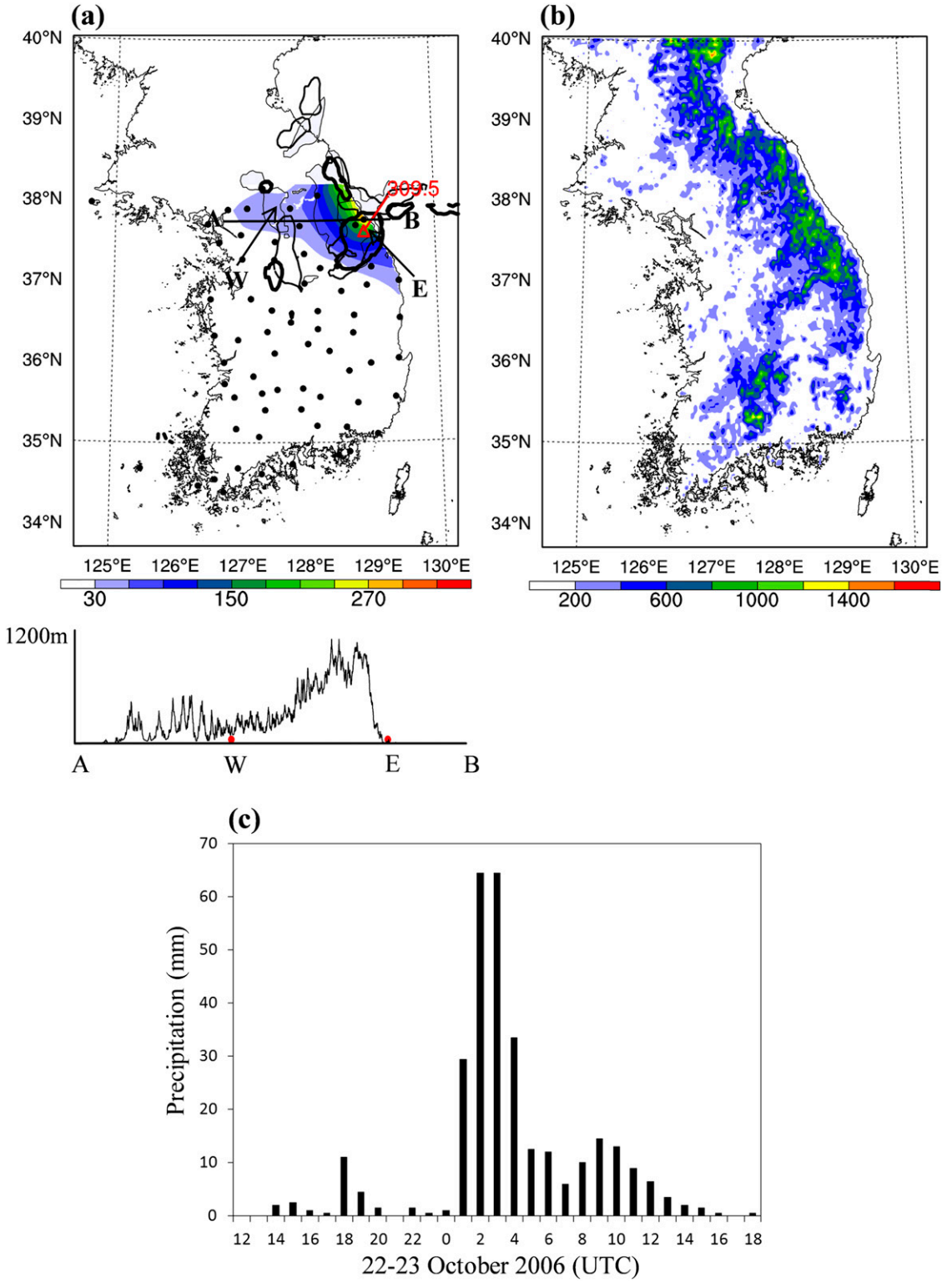

FIG. 2. (a) The observed rainfall amount (mm; shaded) accumulated from 1200 UTC 22 to 1800 UTC 23 Oct, and the reflectivity (dB*Z*; lines) at a 3-km height at 0200 (thin lines), 0300 (semi-thick lines), and 0400 UTC (thick lines) along with topography (to 1200 m) along the line A–B with the locations of the strong-reflectivity region marked W and E. The red triangle denotes the location of Gangneung station. See text for additional description of features. (b) Topography (m) over the Korean Peninsula and (c) hourly precipitation (mm) at Gangneung station.

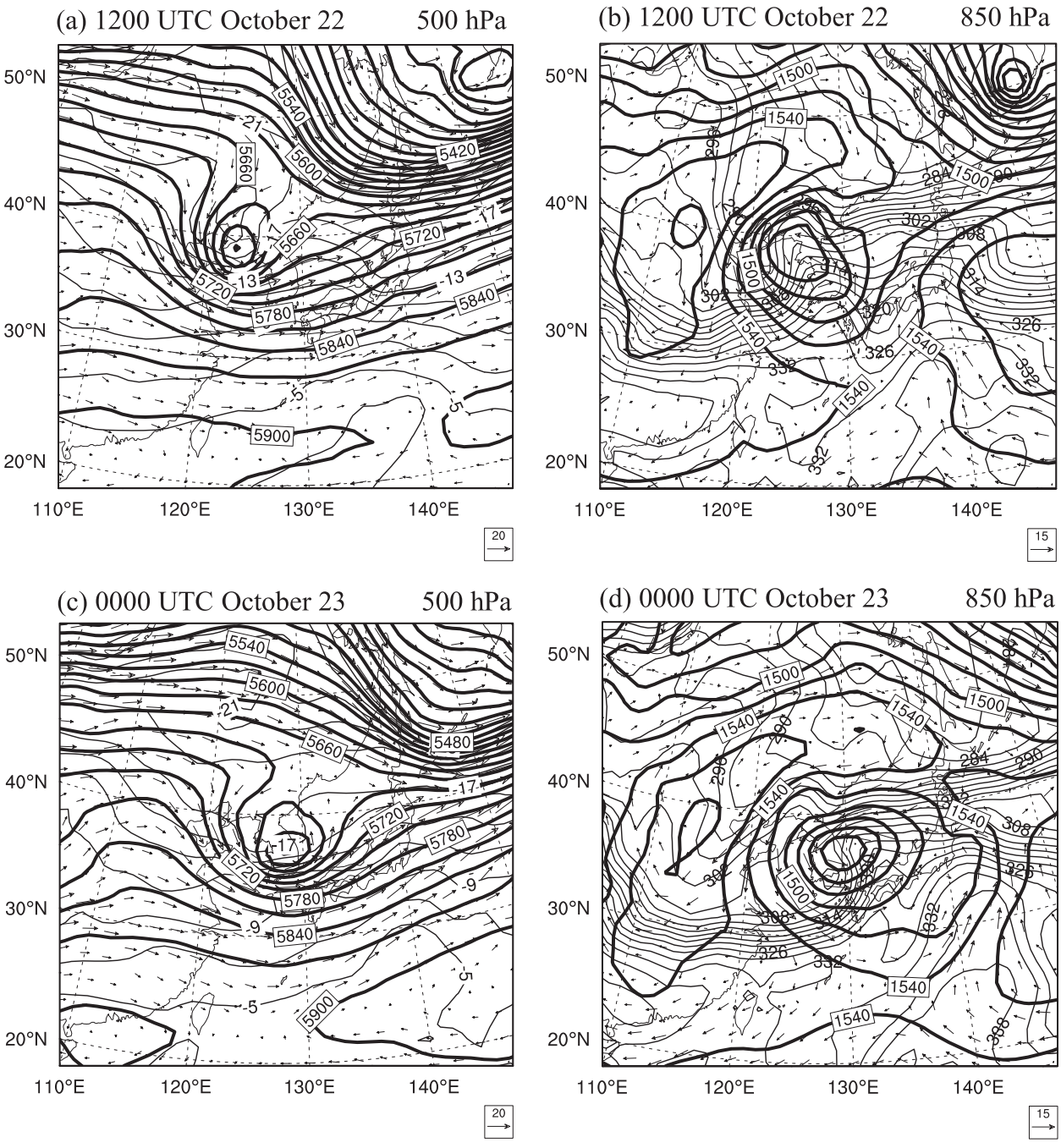

FIG. 3. (a),(c) The 500-hPa geopotential height (gpm; thick solid), temperature (°C; thin solid), and wind vectors ($m\,s^{-1}$). (b),(d) The 850-hPa geopotential height (gpm; thick solid), equivalent potential temperature (K; thin solid), and wind vectors ($m\,s^{-1}$).

respectively. At 1200 UTC 22 October, a low pressure system accompanying a cold core developed over northern China in the 500-hPa chart (Fig. 3a), and a localized low pressure system linked with the 500-hPa low pressure system was located northwest of the Korean Peninsula in the 850-hPa chart (Fig. 3b). During 12 h, the low pressure system moved southeastward up to the northeastern part of the Korean Peninsula (Figs. 3c and 3d). At 0000 UTC 23 October, a deep thermal trough that originated in northern China extended toward southern China with a major axis trending northeast–southwest. The area of high equivalent potential temperature above 308 K extended to the heavy rainfall region along the low pressure system, so that strong

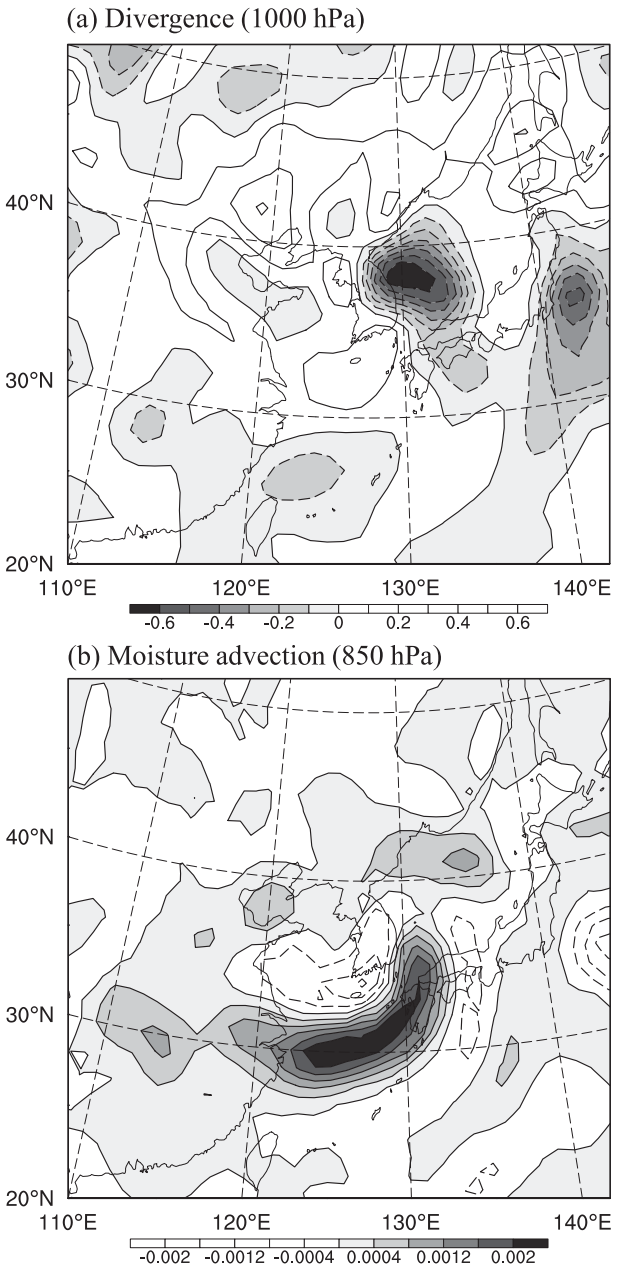

FIG. 4. FNL analysis chart for (a) 1000-hPa divergence ($10^{-4}\,s^{-1}$; negative areas are shaded), and (b) moisture advection at 850 hPa ($10^{-4}\,kg\,kg^{-1}\,s^{-1}$; positive areas are shaded) at 0000 UTC 23 Oct.

baroclinicity built up over the Korean Peninsula and the surrounding vicinity. The 1000-hPa-level divergence and 850-hPa-level moisture advection at 0000 UTC 23 October showed that the low-level convergent area dominated from the northeastern part of the Korean Peninsula to the East Sea (Sea of Japan), and the moisture advection dominated from southern China to the heavy rainfall region with the major axis in the northeast–southwest direction, consistent with the area of high equivalent potential temperature. In contrast, the Korean Peninsula was dominated by dry advection (Figs. 4a,b). This indicates that, in this case, the heavy rainfall was strongly affected by the development of a synoptic-scale system, and the low pressure system played an important role in the development of the convective system by providing warm and moist air at the lower levels over the affected regions.

b. Numerical model and experiment design

The WRF and WRF 3DVAR system (version 3.4.1) was used to assess the potential impact of GPS RO data on predicting the development of this heavy rainfall event. The model is compressible and nonhydrostatic, and thus it is sufficient to depict the convective system associated with a heavy rainfall. We performed the simulations using a twofold one-way nesting system with two model domains of 36 km (230 × 190 horizontal grid points) and 12 km horizontal resolution (373 × 210 horizontal grid points) (Fig. 1). In the vertical direction, there are 38 η model layers, and the model top is 50 hPa. The initial and boundary conditions for the outermost grid domain were provided by linear temporal interpolations of the 6-h FNL analyses. The outer model domain provided the initial and boundary conditions to the nested grid domain. Simulations of the outermost domain and nested domain were carried out for 66 and 30 h, starting at 0000 UTC 21 and 1200 UTC 22 October 2006, respectively. The model simulations employed the cumulus parameterization of the modified version of the Kain–Fritsch scheme and the cloud microphysics scheme of the WRF single-moment 6-class (WSM6). The YSU scheme, Noah land surface model and Rapid Radiative Transfer Model (RRTM) longwave–Dudhia shortwave schemes were used for the planetary boundary layer, land surface, and atmospheric radiation process, respectively. The vertical layers and all model physics were the same in all domains.

Three experiments were conducted: control (hereinafter, CTRL), GPS, and GPS+GPSPW. The CTRL experiment assimilated the conventional measurements. The GPS experiment was identical to the CTRL, except that GPS RO refractivity profiles were additionally assimilated with the local refractivity observation operator in the WRF 3DVAR. All assimilation experiments were performed with continuous cycling of a 6-h assimilation window for a 36-km-horizontal-resolution grid, which could improve the predictability in the nested domain by providing a better synoptic-scale environment and forcing. The number of GPS RO soundings available for each 6-h period is shown in Fig. 1c. For each cycling, the background fields in the subsequent were provided with a 6-h WRF forecast that had been initialized with the

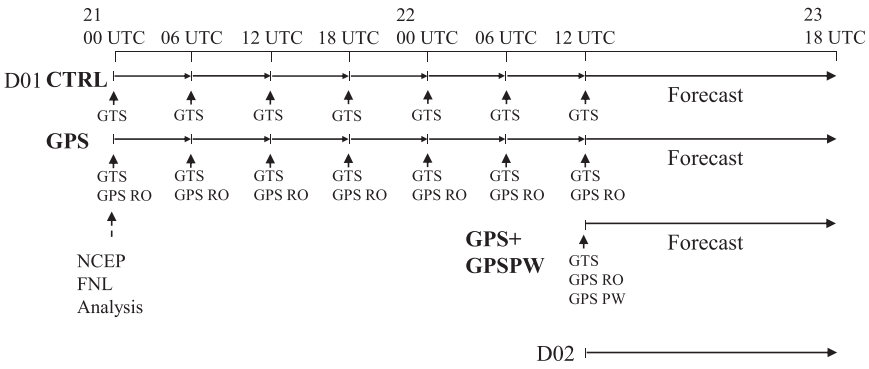

FIG. 5. Schematic diagram of the experimental design illustrating the data assimilation cycle and forecast.

WRF 3DVAR analysis. From the second cycle, the CTRL and GPS experiments used different background fields resulting from the previous cycle of their own experiment. We performed continuous assimilation up to 36 h from 0000 UTC 21 to 1200 UTC 22 October 2006, including a total of seven analysis-update cycles, then 30-h forecasts were produced from 1200 UTC 22 to 1800 UTC 23 October 2006 (Fig. 5). In addition, to examine the impact of assimilating GPS RO refractivity and GPS PW data in the GPS+GPSPW experiment, GPS PW data were added to the GPS experiment at 1200 UTC 22 October 2006 and 30-h forecasts from 1200 UTC 22 October were produced. The background field in GPS+GPSPW was identical to that in GPS. The cycling experiment using GPS RO refractivity and GPS PW data for this case indicated that the rainfall verification does not surpass the GPS+GPSPW experiment, and the results are not shown in this paper. We speculate that the major characteristics of the low pressure system and its rainfall could not be established from previous 3DVAR analyses. This could be due to the long assimilation frequency, that is, a 6-h analysis cycle coupled with a long assimilation window for precipitable water (36 h).

Besides the first guess and observations, another important input for the WRF 3DVAR is the background error covariance matrix. To calculate the background error statistics, we carried out 12- and 24-h forecasts using WRF from 0000 UTC 1 to 1200 UTC 30 October 2006 with 12-h time intervals. The model configuration for the background error statistics was identical to the one for the numerical experiment mentioned above. The average forecast differences (month-long series of 24-h minus 12-h forecasts valid at the same time) were calculated to estimate the background error using the so-called National Meteorological Center method (Parrish and Derber 1992).

4. Numerical results

a. *Analyses with GPS RO refractivity data assimilation*

Figure 6 shows a comparison of a fractional difference defined as $100\% \times (S_{obs} - S_{mod})/S_{obs}$, where S_{obs} and S_{mod} are the observed refractivity and a corresponding model counterpart (background or analysis), during the 36-h cycling assimilation of refractivity profiles for the GPS experiment. In general, the statistics of the difference between observation and background (hereinafter referred to as O−B), and the difference between observation and analysis (hereinafter referred to as O−A) provided useful diagnostic information on the effectiveness of assimilation. Ma et al. (2011) used the same parameter to evaluate the GPS impact on an intense atmospheric river event. Figures 6a and 6b present the statistics for the levels below 10 km for the time period from 0000 UTC 21 to 1200 UTC 22 October 2006. A total of 12 363 observations were used during this period since GPS observation data at each level for each individual sounding were considered as one independent observation. The fractional differences between the observations and model forecasts in Fig. 6a varied from approximately −9.6% to 10.4%, while, the minimum and maximum departures in Fig. 6b ranged from approximately −2.7% to 2.5%. The statistics indicated that O−A (Fig. 6b) had a smaller departure than O−B (Fig. 6a). To examine the performance of GPS RO refractivity data assimilation at different atmospheric levels, the same statistics are also presented for altitudes below 5 km (Figs. 6c,d), and between 5 and 10 km (Figs. 6e,f). More GPS RO data were available for altitudes above 5 km (6963 observations) than below (5400 observations), but the statistics for altitudes above and below 5 km also show good performance of GPS RO refractivity data assimilation with the local observation operator, indicating that this suggests good agreement

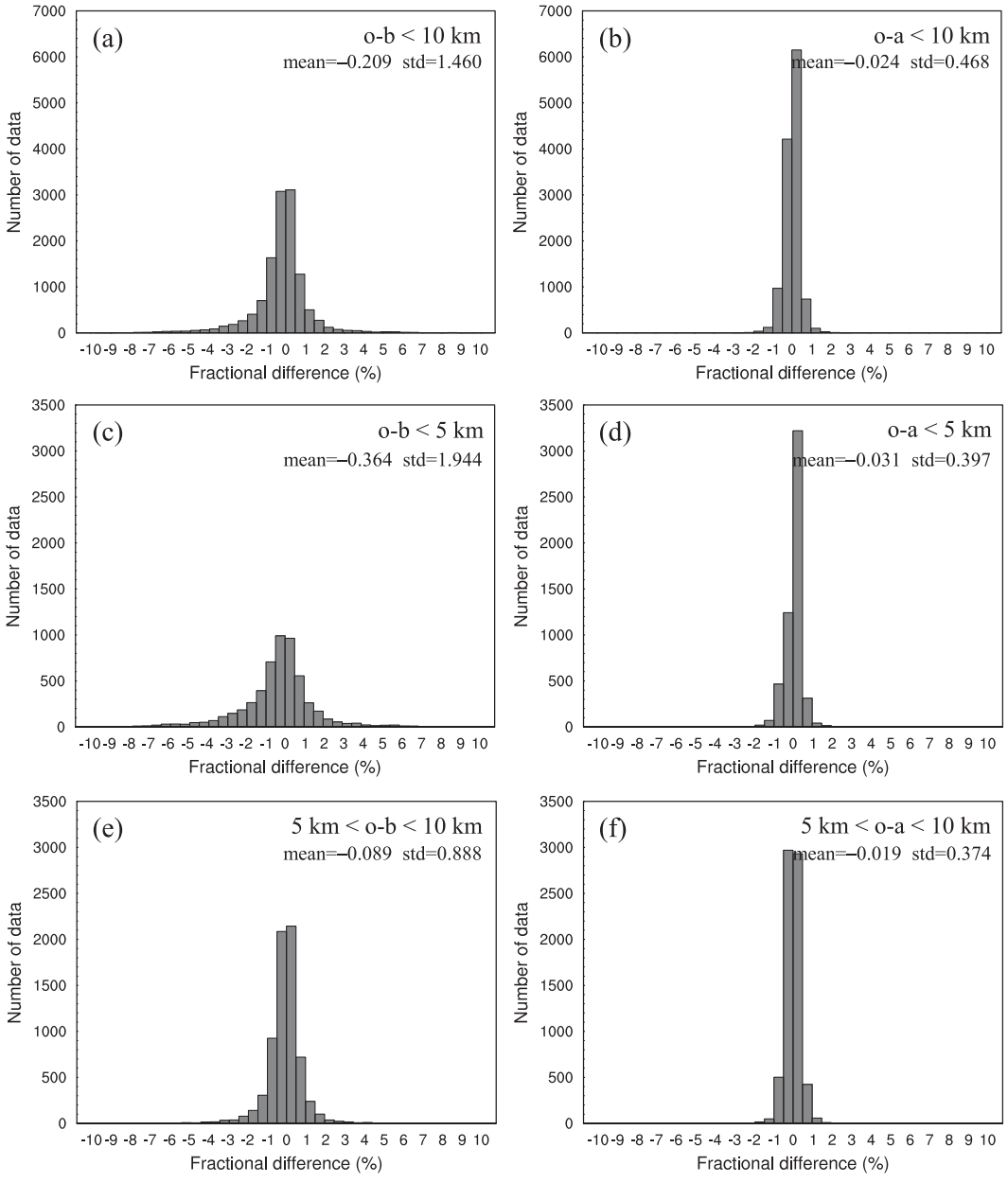

FIG. 6. The fractional difference (%) [(a),(c),(e) O−B; (b),(d),(f) O−A] in the cycling assimilation for (top) below 10 km, (middle) below 5 km, and (bottom) above 5 km.

with the minimization algorithm of the WRF 3DVAR system for GPS RO refractivity data. Comparing the results below and above 5 km, the fractional differences between O−B and O−A for altitudes below 5 km showed similar values to those for altitudes below 10 km (Figs. 6c,d). However, for above 5 km, O−B varied from approximately −6.6% to 6.2% whereas O−A ranged from approximately −2.3% to 2.4%. In addition, from the statistics of mean and standard departures, we found that that the improvement with the GPS RO refractivity data assimilation was more obvious in the lower troposphere (below 5 km) than in the upper troposphere (above 5 km) for this heavy rainfall case, which was consistent with the results in Ma et al. (2011).

Figure 7 shows the domain-averaged analysis error in the outermost domain at the start and end of the assimilation window, valid at 0000 UTC 21 and 1200 UTC 22 October 2006, respectively. Here the analysis error is defined as the root-mean-square error (RMSE) against verifying NCEP FNL analysis. At the first cycle of

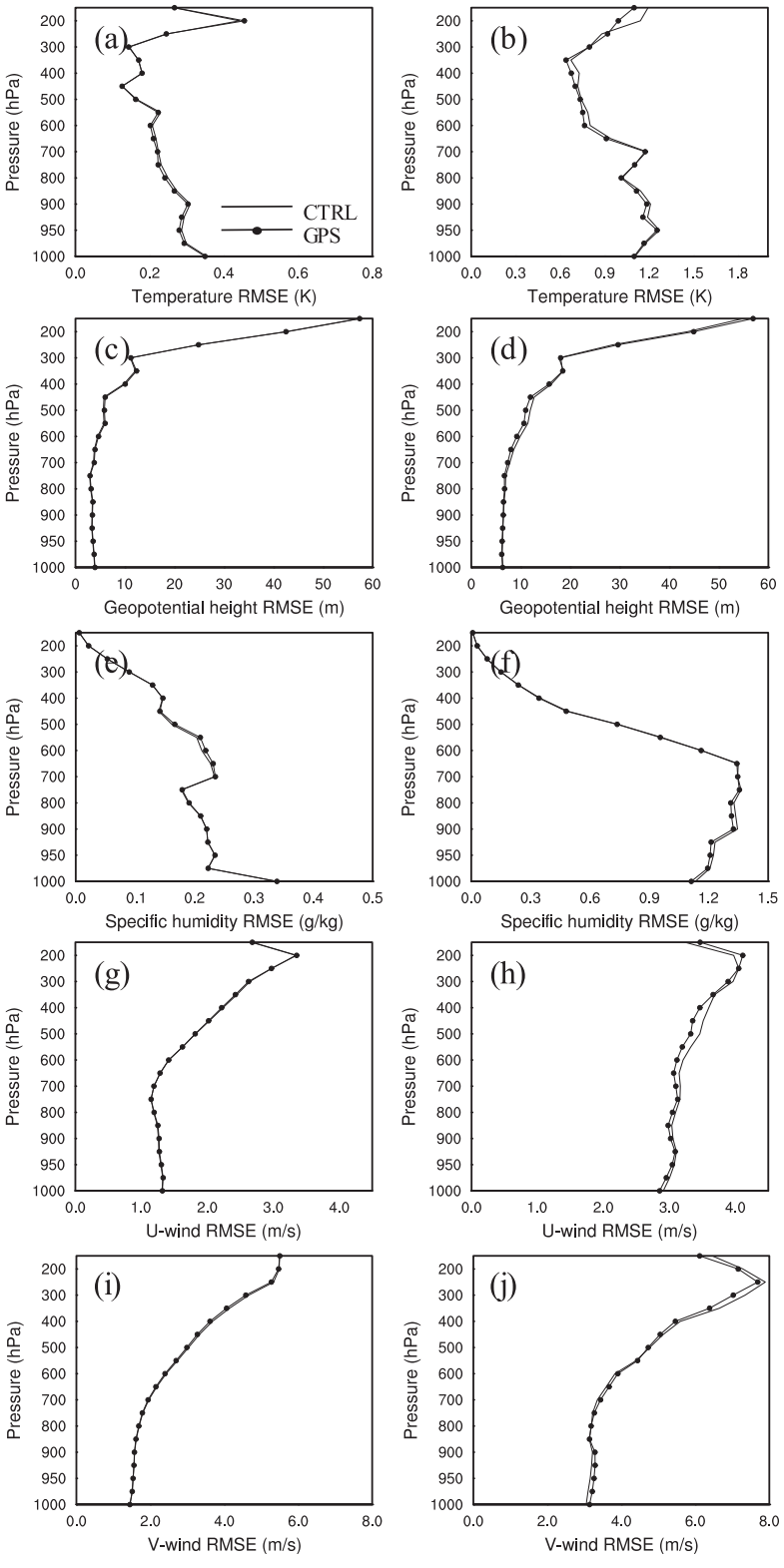

FIG. 7. Vertical distribution of (a),(b) temperature, (c),(d) geopotential height, (e),(f) specific humidity, (g),(h) zonal wind, and (i),(j) meridional wind RMSE in the analysis field at (left) 0000 UTC 21 and (right) 1200 UTC 22 Oct 2006 for CTRL (solid line) and GPS (solid line with dots).

the assimilation, the RMSEs between two experiments were almost the same in magnitude for all vertical levels (Figs. 7a,c,e,g,i); however, it is clear that the RMSEs in the GPS experiment were smaller than those in the CTRL experiment at 1200 UTC 22 October 2006 (Figs. 7b,d,f,h,j). Therefore, the additional information from the cycling run of the GPS RO data assimilation may have led to a significant reduction in analysis errors as compared with the cold start run because applications of cycling analysis overcome the relatively low observational density of GPS RO data. On the other hand, the GPS RO refractivity data assimilation influenced the error reduction in temperature at all the levels, geopotential height below about 350 hPa, and specific humidity below about 600 hPa, which is consistent with the results shown in Fig. 6. This may suggest a hydrostatic response of the mass field to the temperature change by the GPS RO data assimilation, and indicate that the improved geopotential height in the GPS experiment represents more accurate positioning of low pressure system, which results in the improved moisture field that is largely driven by the atmospheric circulation. In addition, the change in the mass field accompanied corresponding change in the winds via the dynamic linkage, and therefore the RMSEs of zonal and meridional winds were reduced by the GPS RO data assimilation. The error reduction of winds was concentrated in the middle and upper troposphere. In the temperature field, the error reduction of temperature was concentrated in the upper troposphere from 250 to 150 hPa, which exhibited differences in performance as compared with the other variables, even though the RMSE at most levels was reduced by the GPS RO data assimilation. This result is consistent with the global model performance of the GPS RO data at the European Centre for Medium-Range Weather Forecasts (ECMWF; Healy 2008). These results again support that the GPS RO refractivity data assimilation using the local observation operator contributed positively to the analysis fields for this heavy rainfall event. Another notable feature in Fig. 7 is that the RMSEs of the geopotential height were larger in scale and remained unchanged in shape with time, which indicates that the geopotential height was slowly varying.

The resultant changes in the analysis due to the inclusion of GPS RO are evaluated in Fig. 7; however, the GPS RO refractivity data assimilation would result in very different changes in model state variables depending on the relative background errors assigned to those variables. Therefore, to evaluate the impact of the GPS RO on the model variables, a normalized sensitivity parameter s is calculated to remove system dependency. The normalized sensitivity is defined as follows:

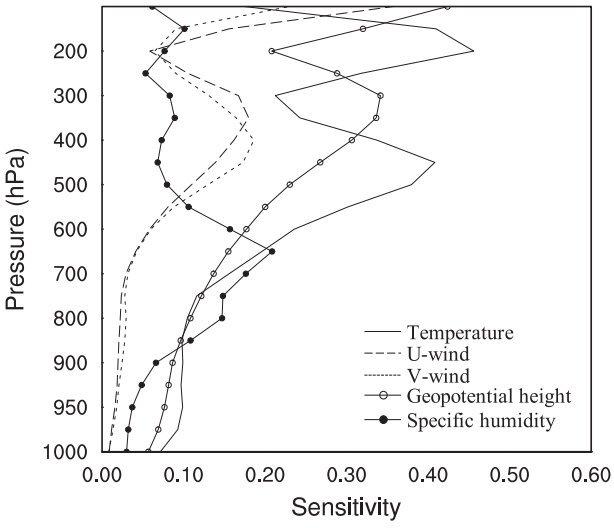

FIG. 8. Sensitivity of 3DVAR assimilation to GPS RO data in temperature (solid line), zonal (short-dashed line) and meridional (long-dashed line) winds, geopotential height (solid line with open circles), and specific humidity (solid line with filled circles) at 0000 UTC 21 Oct 2006.

$$s = \mathrm{rmse}(x_{\mathrm{GPS}}, x_{\mathrm{CTRL}})/\mathrm{rmse}(x_{\mathrm{GPS}}, x_b), \qquad (2)$$

where x_{GPS} is the analysis obtained from the GPS RO data assimilation, x_{CTRL} is the analysis obtained from the conventional data assimilation, and x_b is the background field for the GPS RO data assimilation. Therefore, rmse(x_{GPS}, x_{CTRL}) represents the RMSE between the CTRL and GPS experiments, and rmse(x_{GPS}, x_b) is the RMSE between the analysis and the background field for the GPS experiment. The normalized sensitivity in Eq. (2) is advantageous for comparing the impact of GPS data on different variables in the presence of other observations. Several studies have used the same parameter to evaluate forecast impact (Zapotocny et al. 2002; Wee et al. 2008). Figure 8 shows the normalized sensitivity of the GPS RO data assimilation, averaged over the East Asia area (100°–160°E and 2°–50°N) at 0000 UTC 21 October 2006. The geopotential height, temperature, and winds showed similar structure, and the magnitude of sensitivity in the winds was comparable with that in the temperature and geopotential height. This again demonstrates that the assimilation of GPS RO refractivity data can induce wind changes via the model dynamics. Comparing variables, in the upper troposphere the GPS RO data assimilation was sensitive to the temperature as compared with the other variables, which is consistent with Fig. 7, and the sensitivity for specific humidity showed larger values in the lower troposphere. These results suggest that the assimilation

of GPS RO refractivity data tended to change moisture more easily in the lower troposphere, and hence GPS RO data provided more useful moisture information in the lower troposphere to improve the WRF analysis in this heavy rainfall case.

Figure 9 shows the WRF 3DVAR analysis increment response to the GPS RO data at the end of the assimilation window, valid at 1200 UTC 22 October 2006, to understand the impact of GPS RO data for this heavy rainfall event. Figure 9a shows the increment distributions of the winds and temperature at 500 hPa and Fig. 9b is the increment of the winds and water vapor mixing ratio at 850 hPa. When the GPS RO data assimilation was added, the cyclonic circulation over the West (Yellow) Sea is enhanced in the 500-hPa level; thus the temperature increments present a negative value. In the 850-hPa level, with the assimilation of GPS RO data, GPS experiment produces additional low-level circulation with a low pressure centered near the West Sea as indicated in the black box, and the northwest–southeast-oriented high moisture region is extended to the west coast. The analyses of the increments agree well with the observations (Figs. 3a,b), and therefore from these results we infer that the GPS RO data assimilation is helpful for establishing the tropospheric environment as favorable for this heavy rainfall event.

b. *Skill of precipitation forecast*

Because we observed more moisture modifications at the lower levels by the assimilation of GPS RO soundings, it is of interest to see whether rainfall prediction may be improved. Figures 10a and 10b show the 30-h rainfall accumulation generated by CTRL and GPS using 36-km horizontal resolution from 1200 UTC 22 to 1800 UTC 23 October 2006 after cycling seven times without and with GPS RO refractivity data assimilation, respectively. CTRL did not produce the correct precipitation location and amount when compared with the observed rain (Figs. 2a, 10a). CTRL generated a southward-shifted rainband with about 83.5-km rainfall position error and considerably weaker rainfall amount (239.7 mm). However, GPS generated the correct rainband with the increased rainfall amount in the northeastern part of the Korean Peninsula (280.1 mm) and reduced rainfall position error (32.0 km), even though some erroneous precipitation was simulated in the southern part of the Korean Peninsula and the maximum precipitation was underestimated compared with the observation (309.5 mm) (Fig. 10b). In terms of time series of hourly rainfall at the maximum precipitation point, the evolution of hourly rainfall in GPS was similar to that in CTRL, in which the rainfall peak was delayed by approximately 5 h when compared with the observed rainfall peak (Fig. 11). These results suggest that the GPS RO data contributed to the improvement of the rainfall distribution and amount, not the time of the heavy rainfall onset.

Several studies (Anthes et al. 1985; Weisman and Trapp 2003) suggested that accurate large-scale forcing as lateral boundary conditions can significantly reduce error growth for high-resolution limited-area models, because the large-scale information constantly sweeps through the inflow boundaries. Therefore, we investigated whether the GPS RO data assimilation, which improved the analysis and forecast in the outermost domain, would influence the predictability of rainfall in the 12-km-resolution domain. Figure 12 shows the 30-h accumulated rainfalls using 12-km horizontal resolution from 1200 UTC 22 to 1800 UTC 23 October for CTRL and GPS. In the simulations, the rainfalls in both experiments tended to increase as compared with the simulated rainfalls using 36-km horizontal resolution; in particular, the amount of rainfall in the northern part of Gangneung was increased (Figs. 12a,b). Between the two experiments, the rainfall distribution in GPS corresponded with the observed rain to some extent, even though it expanded the rainfall region along the east coast with local maxima of 354.1 and 305.3 mm, and overestimated the rainfall amount. In contrast, CTRL produced a rainband that shifted southward, and the amount of rainfall in the western and southern part of Gangneung increased, which was in disagreement with the observed rain. From the two assimilation experiments in the 36- and 12-km grid domain, it appeared that the observed rainfall maximum on the northeastern part of the Korean Peninsula was better captured by GPS. To investigate the ability of the model at quantitative precipitation forecast (QPF), threat scores for the two experiments were calculated (Fig. 13). The threat scores at the 1- and 10-mm thresholds showed similar values between the experiments because the land area with these threshold values was comparable in the two experiments. However, the experiment with GPS RO data assimilation produced higher threat scores than CTRL for heavy rainfall (thresholds of 30 and 50 mm) in all model domains because of the improved amount and location of the heavy rainfall, illustrating that the dominant impact of GPS RO data assimilation is on heavier precipitation. Bias scores for GPS were also better than GTS (not shown here). For this heavy rainfall case, GPS RO data assimilation resulted in an improved short-range forecast skill for heavy precipitation.

To look into details of the impact of GPS data on the simulated local circulation, Fig. 14 shows the zoomed differences in the equivalent potential temperature and wind vectors at 850 hPa, and the temperature and wind

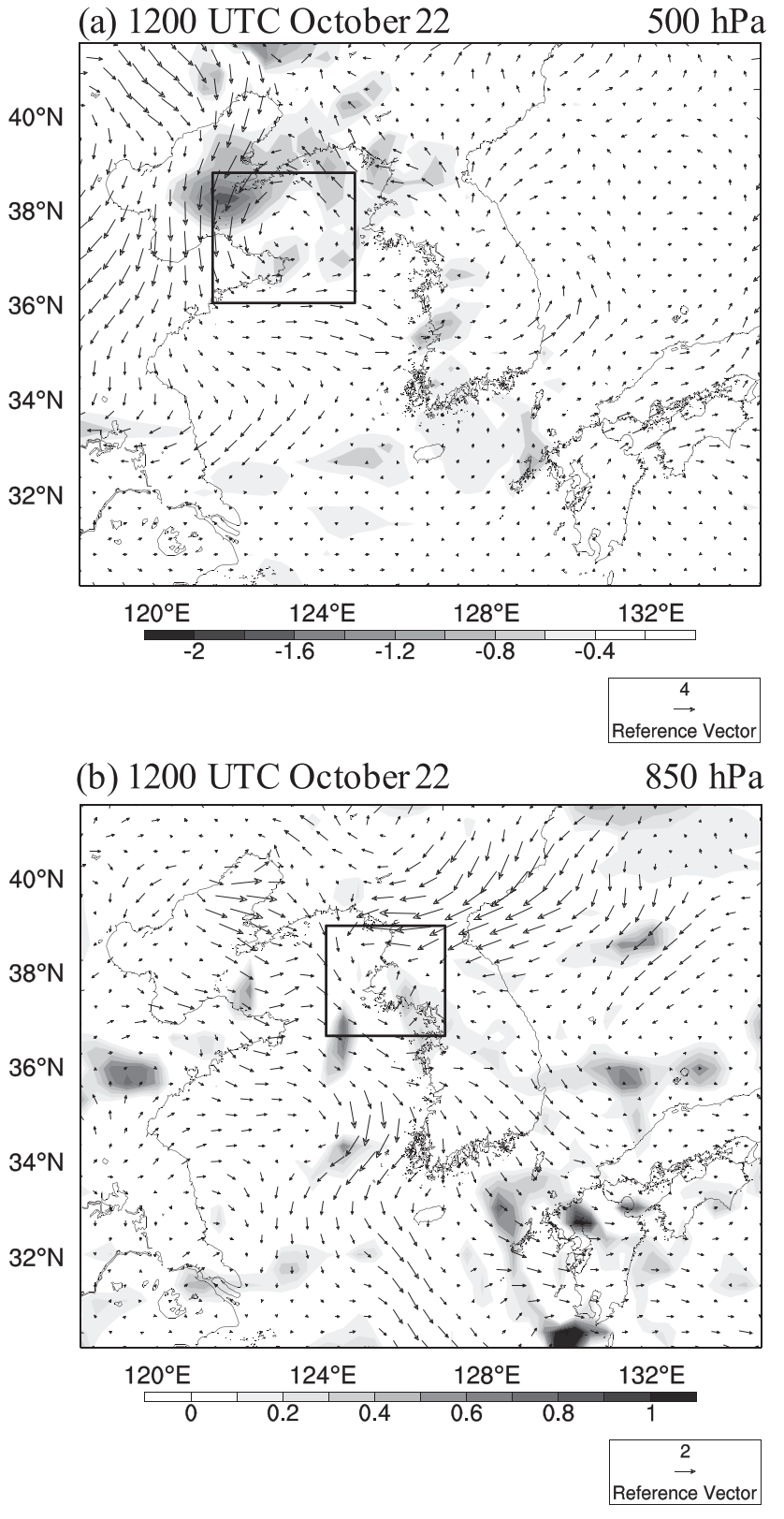

FIG. 9. The WRF 3DVAR analysis increment response to the GPS RO data: (a) winds ($m\,s^{-1}$; arrows) and temperature (K; shaded) at 500 hPa, and (b) winds ($m\,s^{-1}$; arrows) and water vapor mixing ratio ($g\,kg^{-1}$; shaded) at 850 hPa at 1200 UTC 22 Oct 2006.

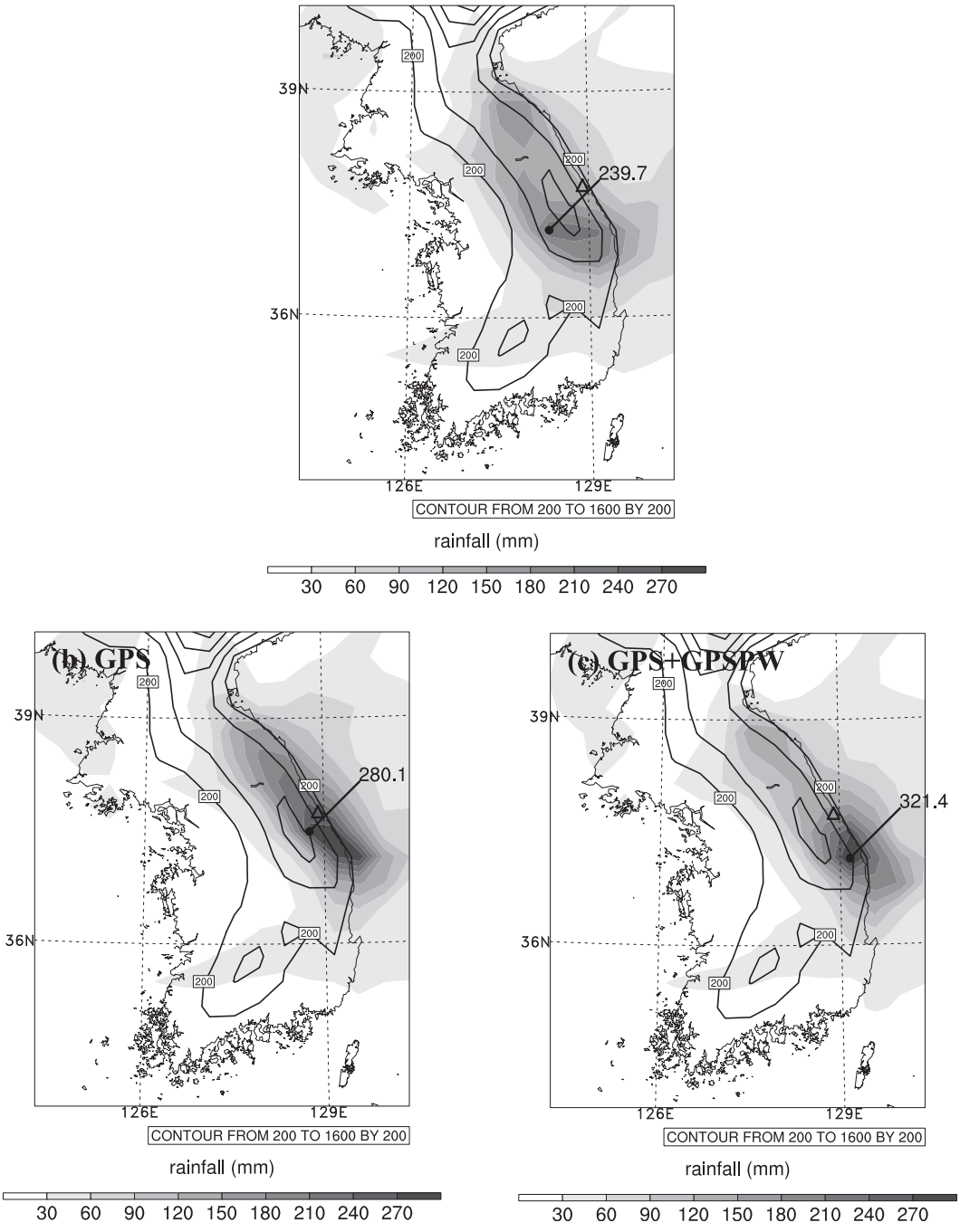

FIG. 10. Total accumulated 30-h rainfall (mm; shaded) using 36-km-horizontal-resolution grid from 1200 UTC 22 to 1800 UTC 23 Oct 2006 for (a) CTRL, (b) GPS, and (c) GPS+GPSPW with topography (solid lines).

vectors at 500 hPa between CTRL and GPS at 0300 UTC 23 October 2006. This is about 3 h before the intense rainfall occurred in the simulated rainband for the outermost domain. In the two experiments, the experiment with GPS RO data assimilation produced significant effects on the establishment of a favorable tropospheric environment for this heavy rainfall, which is consistent with the result of the analysis increments. The local circulation with a low pressure centered near the east coast in the lower troposphere was much more similar for GPS than CTRL (Fig. 14a). Indeed, CTRL produced a westward-biased circulation, with a weakened low pressure center. Moreover, in the difference of equivalent potential temperature, the positive difference in the

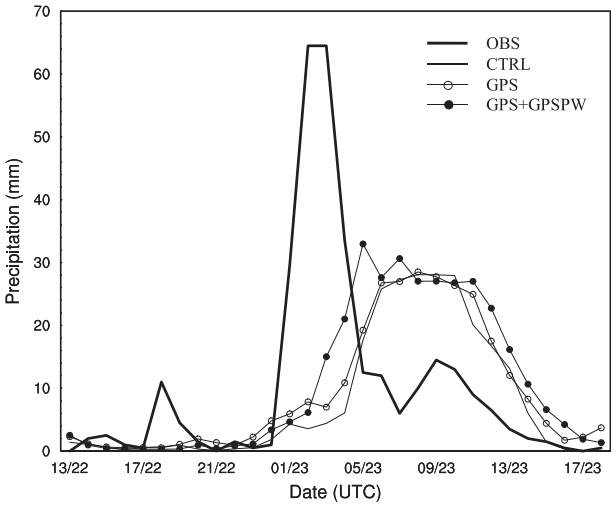

FIG. 11. Time series of the observed and simulated hourly precipitation (mm) at the grid point of the maximum accumulated 30-h rainfall.

East Sea and the negative difference over the central Korean Peninsula appeared to follow the cyclonic circulation. This demonstrates that the GPS RO data assimilation contributed to the distribution of the water vapor over the Korean Peninsula and the surrounding vicinity. At 500 hPa, the northerly or northwesterly flow in the West Sea was enhanced when the GPS data assimilation was added, and therefore the cold air dominated over the Korean Peninsula to follow this flow. These results correspond with the observations in Figs. 3 and 4; note that the GPS RO data played an important role in inducing the tropospheric environment to be favorable for heavy rainfall by representing more accurate positioning of a low pressure system affecting the distribution of water vapor.

c. *Impact of GPS RO data and ground-based GPS PW data*

Besides the GPS RO data assimilation, assimilation methods of ground-based GPS data, including PW, have been developed and several studies have shown a positive impact of GPS PW data assimilation on the weather predictions (Seko et al. 2004; Koizumi and Sato 2004; Kwon et al. 2010). Although the impacts of GPS RO data and ground-based GPS PW data are investigated individually, there have been very few studies so far of the impact of simultaneous assimilations with these data on the heavy rainfall event. Both data are expected to give complementary information about the water vapor in our model domain. Therefore, in this section, the impact of simultaneous assimilations of GPS RO data and ground-based GPS PW data, namely, GPS+GPSPW, is investigated.

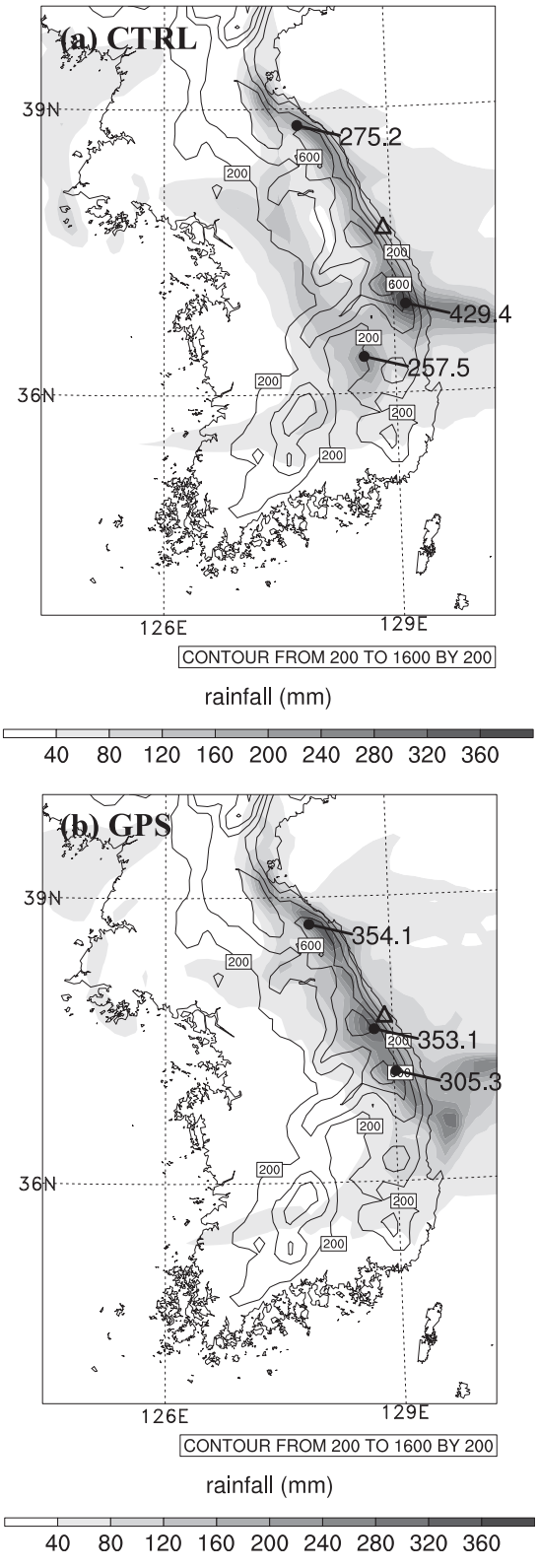

FIG. 12. Total accumulated 30-h rainfall (mm) using 12-km-horizontal-resolution grid from 1200 UTC 22 to 1800 UTC 23 Oct for (a) CTRL and (b) GPS with topography (solid lines).

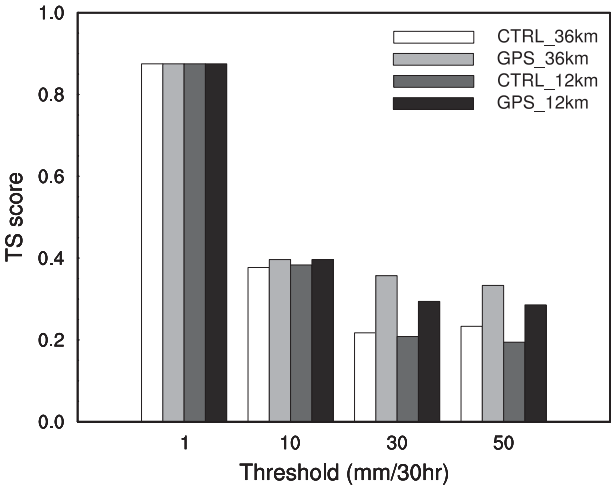

FIG. 13. Threat scores for the accumulated 30-h amount of precipitation from 1200 UTC 22 to 1800 UTC 23 Oct in the CTRL and GPS experiments.

Incorporation of the GPS PW produced sizable moisture increments, that is, the differences between the fields with and without GPS PW data assimilations, as shown in Fig. 15a for the 850-hPa level at 1200 UTC 22 October 2006. In the difference field, the assimilation of GPS PW decreased the moisture over the central Korean Peninsula and increased the moisture over the south of Japan, leading to an enhanced moisture gradient in the lower troposphere when the GPS PW data were added to the data assimilation. Further, these difference fields coincided with the low-level moisture advection and dry advection regions in Fig. 4b. However, the assimilation of GPS PW data caused marginal increments in temperature over the central Korean Peninsula (not shown here), and hence the responses of the wind increments were generally weak, as is typical of the associated small temperature changes with a hydrostatic balance in 3DVAR (Huang et al. 2005). When RO data and ground-based GPS PW data were assimilated simultaneously, the moisture field was also improved vertically as shown in Fig. 15b. Figure 15b shows the average difference of RMSE against verifying NCEP FNL analysis (GPS+GPSPW minus GPS), which means the error reduction due to assimilation of GPS PW data, in the 36-km grid domain. Even though the magnitude of the error reduction was relatively small because of the low observational density of GPS PW data (Fig. 1b), the error reduction of the moisture by the assimilation of GPS PW data was concentrated in the lower troposphere below about 600 hPa, which can be important in the predictability of the precipitation system. When GPS RO data and GPS PW data were assimilated simultaneously, the moisture fields were further improved horizontally and vertically as compared with the experiment that included only GPS RO data assimilation. This improvement of analysis affected the rainfall prediction in GPS+GPSPW (Figs. 9c, 10). With regard to the rainfall distribution, it was difficult to assess which experiment performed better, since there were no rainfall observations over the northern Korean Peninsula and rainfall distributions in both experiments were similar. However, in comparison with the observations (Fig. 2a), we can see that in GPS+GPSPW, the area with intense rainfall greater than 150 mm was more localized over the northeastern part of the Korea Peninsula, and maximum rainfall amounts for GPS+GPSPW was roughly 40 mm greater than that of GPS, which was close to the observed rainfall maximum. Although the results of rainfall distribution seem mixed, GPS+GPSPW simulation showed better agreement with the observed rainfall than GPS simulation (Fig. 9c). Furthermore, in the time series of the maximum rainfall point, the simulated rainfall in GPS+GPSPW began in the early hours of the forecast as compared with that in GPS, which demonstrated that GPS PW data assimilation contributed to forecasting the time of the heavy rainfall onset, even though the evolution of hourly rainfall at the maximum rainfall point in GPS+GPSPW was similar to that in GPS (Fig. 10). These results indicate that the GPS PW data facilitated the depiction of the development of convective systems by representing more accurate moisture distribution horizontally and vertically in the lower troposphere. Therefore, using both data sources together resulted in better simulation of this heavy rainfall in GPS+GPSPW than in GPS RO data source only.

5. Summary and conclusions

By using the WRF model in combination with its 3DVAR system, we explored the impact of the GPS RO data from COSMIC and CHAMP missions on the analyses and forecasts of a heavy rainfall event over the Korean Peninsula. We focused on assessing quantitatively the added value of GPS RO data in forecasting the heavy rainfall event on 22–23 October 2006. The results may be summarized as follows:

1) The impact with one-time GPS RO data assimilation was marginal; however, the cycling assimilation of GPS RO data contributed positively to the analysis fields since the problem related to the relatively low observation density of GPS RO data can be partly mitigated by iteration. Inspection of the changes in the analysis due to the assimilation of GPS RO data revealed that GPS RO data had a large impact on the

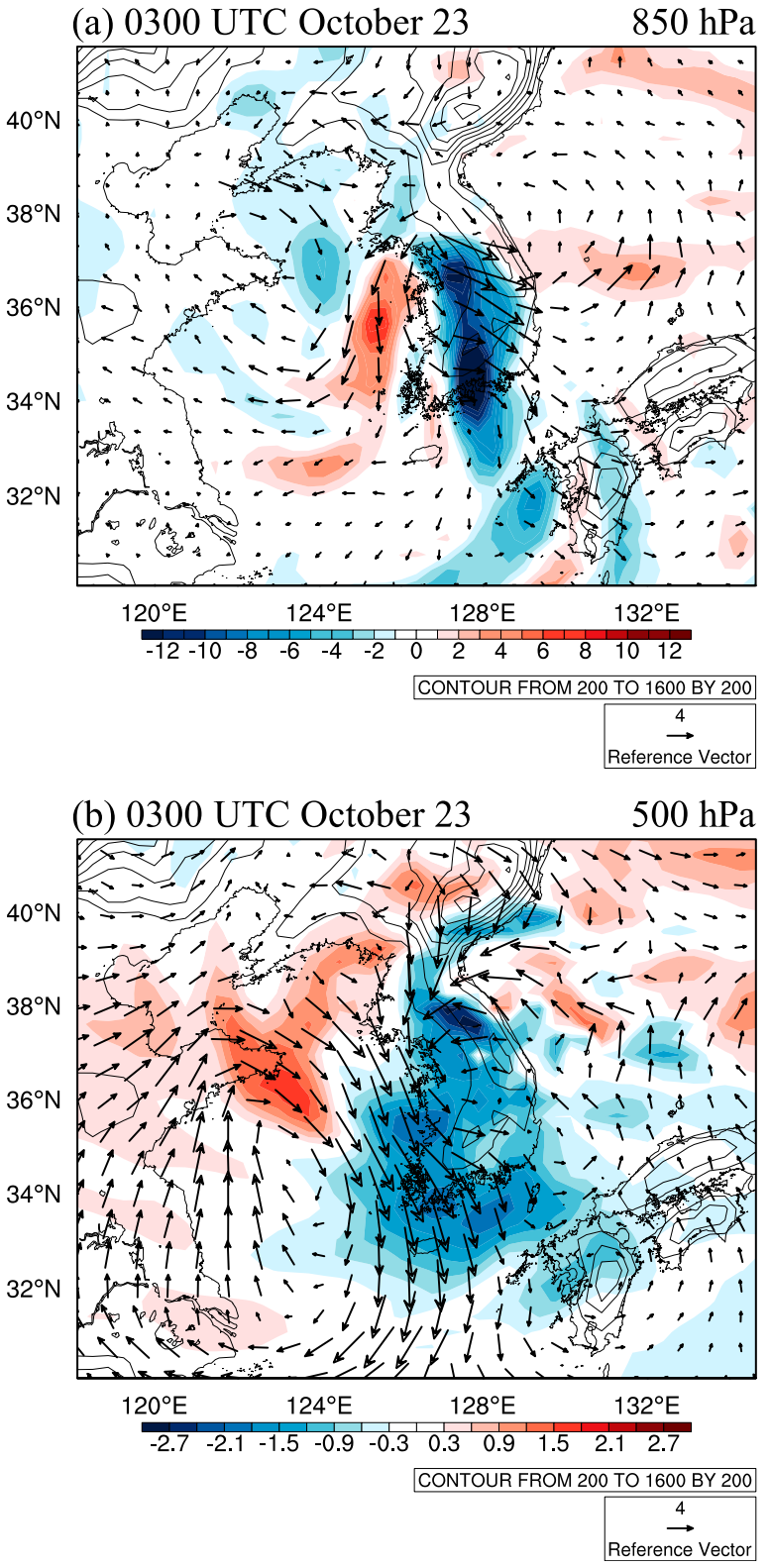

FIG. 14. GPS difference from CTRL for (a) 850-hPa equivalent potential temperature (K; shaded) and wind vectors ($m\,s^{-1}$; arrows) and (b) 500-hPa temperature (°C; shaded) and wind vectors ($m\,s^{-1}$; arrows) with topography (solid lines) at 0300 UTC 23 Oct 2006.

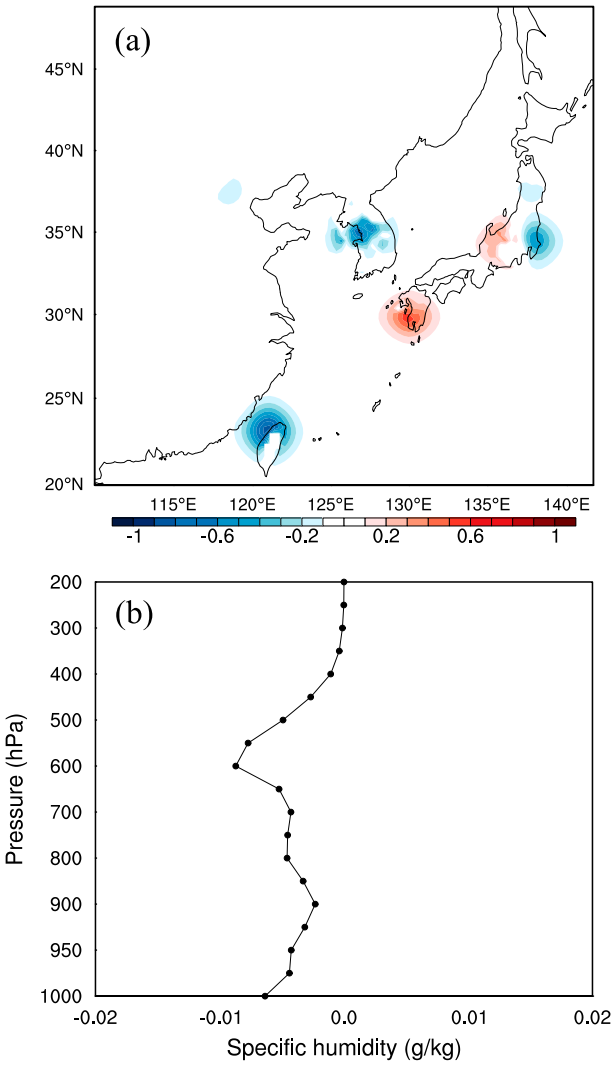

FIG. 15. (a) Initial increment of specific humidity ($g\,kg^{-1}$) at 850 hPa produced by GPS PW data assimilation. (b) Analysis-error difference for GPS+GPSPW run minus GPS run at 1200 UTC 22 Oct 2006. The analysis error is defined as the RMSE difference against the verifying NECP FNL analyses.

moisture distribution in the lower troposphere, and the changes in the mass field by the GPS RO data assimilation accompanied corresponding changes in the winds via the dynamic linkage. Thus, the improvement of precipitation forecast was clearly linked to assimilation of the GPS RO data.

2) In simulations without GPS RO data, neither precipitation amount nor location was captured accurately. In contrast, the assimilation of GPS RO data resulted in a much-improved rainfall forecast. The improvements included a reasonable forecast rainfall distribution and enhanced maximum rainfall amount. The results indicate the potential benefits of GPS RO data on numerical simulations of a heavy rainfall event with the local operator in the WRF 3DVAR system, allowing the 3DVAR system with the GPS RO data assimilation to more accurately represent positioning of the low pressure system. The exact positioning of the low pressure system enhanced the transport of warm and moist air toward the heavy rainfall region. Consequently, this enhanced low-level convergence so that the simulation with the GPS RO data assimilation could identify the location of the observed rainfall with the increased rainfall amount (280.1 mm), although the maximum rainfall amount was still smaller compared with the observed amount (309.5 mm) and the development of the convective system was delayed by approximately 5 h. Similar improvement was also discernible in the quantitative precipitation forecast (QPF), and the improvement of QPF was observed more clearly for heavy rainfall than for light rainfall.
3) The simultaneous assimilation of GPS RO and ground-based GPS PW data can improve the initial structure of moisture and the subsequent precipitation forecasts. The improvements appeared in the strength of the horizontal moisture gradient in the vicinity of the heavy rainfall region, the vertical distribution of moisture, maximum rainfall amount, and the more accurate onset time of the heavy rainfall (but less improvement appeared in the horizontal distribution of rainfall). This result indicates that assimilation of both datasets has a clear advantage in its ability to aid an accurate simulation of the moisture field and to lead to contributing to the depiction of the development of convective system, allowing the 3DVAR system to more effectively extract useful moisture information from GPS PW observations at the initial time.

In this paper, only one case was investigated. It is recommended that additional cases are studied, which would allow an assessment of how representative the results of this case study are to other high-impact events over the Korean Peninsula. In comparison with the simulated rainfalls, experiments with higher horizontal resolution simulated enhanced maximum rainfall amount around the target area when compared with the experiment having lower horizontal resolution that seemed to be increased the topographic height. Thus, in future studies, the topography effect should be investigated using the data assimilation because the previous studies noted that the complicated topography of the Korean Peninsula is an important factor in heavy rainfall development. In addition, the assimilation of more GPS PW data over the Korean Peninsula will be

carried out in the near future to obtain better analysis results and subsequent forecasts. The data assimilation still had limitations in regards to the quality of the GPS data and the balance conditions in the numerical weather prediction model. In this respect, we think that there is still plenty of opportunity for further improvement of data assimilation techniques and data quality for the GPS-derived variables for more accurate forecasts of heavy rainfall events.

Acknowledgments. We acknowledge that this work was funded by the Korea Meteorological Administration Research and Development Program under Grant CATER 2012-6080. This work was also partly supported by the Brain Korea 21 Project.

REFERENCES

Anthes, R. A., Y. H. Kuo, D. P. Baumhefner, R. P. Erico, and T. W. Bettge, 1985: Predictability of mesoscale atmospheric motions. *Advances in Geophysics,* Vol. 28B, Academic Press, 159–202, doi:10.1016/S0065-2687(08)60188-0.

——, and Coauthors, 2008: The COSMIC/FORMOSAT-3 mission: Early results. *Bull. Amer. Meteor. Soc.,* **89,** 313–333, doi:10.1175/BAMS-89-3-313.

Chen, S.-Y., C.-Y. Huang, Y.-H. Kuo, Y.-R. Guo, and S. Sokolovskiy, 2009: Assimilation of GPS refractivity from FORMOSAT-3/COSMIC using a nonlocal operator with WRF 3DVAR and its impact on the prediction of a typhoon event. *Terr. Atmos. Ocean. Sci.,* **20,** 133–154, doi:10.3319/TAO.2007.11.29.01(F3C).

Cucurull, L., Y.-H. Kuo, D. Barker, and S. R. H. Rizvi, 2006: Assessing the impact of simulated COSMIC GPS radio occultation data on weather analysis over the Antarctic: A case study. *Mon. Wea. Rev.,* **134,** 3283–3296, doi:10.1175/MWR3241.1.

Hajj, G. A., and Coauthors, 2004: CHAMP and SAC-C atmospheric occultation results and intercomparisons. *J. Geophys. Res.,* **109,** D06109, doi:10.1029/2003JD003909.

Healy, S. B., 2008: Forecast impact experiment with a constellation of GPS radio occultation receivers. *Atmos. Sci. Lett.,* **9,** 111–118, doi:10.1002/asl.169.

Huang, C.-Y., Y.-H. Kuo, S.-H. Chen, and F. Vandenberghe, 2005: Improvements on typhoon forecasts with assimilated GPS occultation refractivity. *Wea. Forecasting,* **20,** 931–953, doi:10.1175/WAF874.1.

Koizumi, K., and Y. Sato, 2004: Impact of GPS and TMI precipitable water data on mesoscale numerical weather prediction model forecasts. *J. Meteor. Soc. Japan,* **82,** 453–457, doi:10.2151/jmsj.2004.453.

Kuo, Y.-H., X. Zou, and W. Huang, 1998: The impact of Global Positioning System data on the prediction of an extratropical cyclone: An observing system simulation experiment. *Dyn. Atmos. Oceans,* **27,** 439–470, doi:10.1016/S0377-0265(97)00023-7.

——, S. Sokolovskiy, R. A. Anthes, and F. Vandenberghe, 2000: Assimilation of GPS radio occultation data for numerical weather prediction. *Terr. Atmos. Ocean. Sci.,* **11,** 157–186.

Kwon, H.-T., E.-H. Jung, and G.-H. Lim, 2010: A comparison of GPS- and NWP-derived PW data over the Korean Peninsula. *Adv. Atmos. Sci.,* **27,** 871–882, doi:10.1007/s00376-009-9069-4.

Liu, H., and X. Zou, 2003: Improvements to GPS radio occultation ray-tracing model and their impacts on assimilation of bending angle. *J. Geophys. Res.,* **108,** 4548, doi:10.1029/2002JD003160.

Ma, Z., Y.-H. Kuo, F. M. Ralph, P. J. Neiman, G. A. Wick, E. Sukovich, and B. Wang, 2011: Assimilation of GPS radio occultation data for an intense atmospheric river with the NCEP regional GSI system. *Mon. Wea. Rev.,* **139,** 2170–2183, doi:10.1175/2011MWR3342.1.

Park, S.-G., and D.-K. Lee, 2009: Retrieval of high-resolution wind fields over the southern Korean Peninsula using the Doppler weather radar network. *Wea. Forecasting,* **24,** 87–103, doi:10.1175/2008WAF2007084.1.

Parrish, D. F., and J. C. Derber, 1992: The National Meteorological Center's spectral-interpolation analysis system. *Mon. Wea. Rev.,* **120,** 1747–1763, doi:10.1175/1520-0493(1992)120<1747:TNMCSS>2.0.CO;2.

Phinney, R. A., and D. L. Anderson, 1968: On the radio occultation method for studying planetary atmosphere. *J. Geophys. Res.,* **73,** 1819–1827, doi:10.1029/JA073i005p01819.

Seko, H., T. Kawabata, T. Tsuyuki, H. Nakamura, K. Koizumi, and T. Iwabuchi, 2004: Impacts of GPS-derived water vapor and radial wind measured by Doppler radar on numerical prediction of precipitation. *J. Meteor. Soc. Japan,* **82,** 473–489, doi:10.2151/jmsj.2004.473.

Smith, E. K., and S. Weintraub, 1953: The constants in the equation for atmospheric refractivity index at radio frequencies. *J. Res. Natl. Bur. Stand.,* **50,** 39–41, doi:10.6028/jres.050.006.

Ware, R., and Coauthors, 1996: GPS sounding of the atmosphere from low earth orbit: Preliminary results. *Bull. Amer. Meteor. Soc.,* **77,** 19–40, doi:10.1175/1520-0477(1996)077<0019:GSOTAF>2.0.CO;2.

Wee, T.-K., Y.-H. Kuo, D. H. Bromwich, and A. J. Monaghan, 2008: Assimilation of GPS radio occultation refractivity data from CHAMP and SAC-C missions over high southern latitudes with MM5 4DVAR. *Mon. Wea. Rev.,* **136,** 2923–2944, doi:10.1175/2007MWR1925.1.

Weisman, M. L., and R. J. Trapp, 2003: Low-level mesovortices within squall-line and bow echoes. Part I: Overview and dependence on environmental shear. *Mon. Wea. Rev.,* **131,** 2779–2803, doi:10.1175/1520-0493(2003)131<2779:LMWSLA>2.0.CO;2.

Wickert, J., and Coauthors, 2001: Atmosphere sounding by GPS radio occultation: First results from CHAMP. *Geophys. Res. Lett.,* **28,** 3263–3266, doi:10.1029/2001GL013117.

Zapotocny, T. H., W. P. Menzel, J. P. Nelson, and J. A. Jung, 2002: An impact study of five remotely sensed and five in situ data types in the Eta Data Assimilation System. *Wea. Forecasting,* **17,** 263–285, doi:10.1175/1520-0434(2002)017<0263:AISOFR>2.0.CO;2.